Large orbital moment and spin-orbit enabled Mott transition in the Ising Fe honeycomb lattice of BaFe$_2$(PO$_4$)$_2$

Young-Joon Song,[1] Kwan-Woo Lee,[1,2,*] and Warren E. Pickett[3,†]

[1]*Department of Applied Physics, Graduate School, Korea University, Sejong 339-700, Korea*
[2]*Department of Display and Semiconductor Physics, Korea University, Sejong 339-700, Korea*
[3]*Department of Physics, University of California, Davis, California 95616, USA*

BaFe$_2$(PO$_4$)$_2$ is an unusual Ising insulating ferromagnet based on the Fe^{2+} spin $S = 2$ ion, the susceptibility of which suggests a large orbital component to the Fe local moment. We apply density functional theory based methods to obtain a microscopic picture of the competing interactions and the critical role of spin-orbit coupling (SOC) in this honeycomb lattice system. The low-temperature ferromagnetic phase displays a half-semimetallic Dirac point pinning the Fermi level and preventing gap opening before consideration of SOC, presenting a case in which correlation effects modeled by a repulsive Hubbard U fail to open a gap. Simultaneous inclusion of both correlation and SOC drives a large orbital moment in excess of 0.7 μ_B (essentially $L = 1$) for spin aligned along the $\hat{c}$ axis, with a gap comparable with the inferred experimental value. The large orbital moment accounts for the large Ising anisotropy, in spite of the small magnitude of the SOC strength on the $3d$ (Fe) ion. Ultimately, the Mott-Hubbard gap is enabled by degeneracy lifting by SOC and the large Fe moments, rather than by standard Hubbard interactions alone. We suggest that competing orbital occupations are responsible for the structural transitions involved in the observed reentrant rhombohedral-triclinic-rhombohedral sequence.

I. INTRODUCTION

In the last few decades, the two-dimensional (2D) honeycomb lattice has attracted interest due to several exotic physical phenomena related with superconductivity, magnetism, and topological phases, and to the Dirac point 2D material graphene. Recently, discoveries of topological insulators, originally on the honeycomb lattice [1], have stimulated increased research on properties of systems with honeycomb lattices [2–4].

Transition-metal d^1 systems are good examples to investigate the interplay among lattice, spin, orbital degrees of freedom, and correlation effects, since variation of $3d \rightarrow 4d \rightarrow 5d$ leads to weakening strength of correlation, but strengthening of spin-orbit coupling (SOC). For $5d^1$ systems, a large SOC results in a $J_{\text{eff}} = \frac{3}{2}$ Dirac (or relativistic) Mott insulator in Ba$_2$NaOsO$_6$ [5,6] in which the orbital moment plays a pivotal role. Similarly, a $J_{\text{eff}} = \frac{1}{2}$ Mott transition has been proposed in $5d^5$ Sr$_2$IrO$_4$, i.e., one hole in the t_{2g} manifold [7]. $4d^1$ systems usually have a reduced SOC and some enhanced correlation strengths. In $3d$ systems, a much stronger correlation strength leads to a Mott transition, which has been intensively discussed [8], while SOC is usually minor. Here, we focus on the recently synthesized BaFe$_2$(PO$_4$)$_2$ compound with a honeycomb lattice of high spin d^6 Fe^{2+} ions, leading to an effectively isolated minority-spin d^1 configuration due to a large exchange splitting of the high spin Fe ion. Large $3d$ orbital moments have been encountered recently [9] in low-symmetry environments but gaining understanding of their origin is not simple.

Mentré and coworkers synthesized a rare example of an insulating 2D Ising ferromagnetic (FM) oxide BaFe$_2$(PO$_4$)$_2$,

confirmed by the observed critical exponents in good agreement with the theoretical Ising values, with the Curie temperature $T_C = 65$ K and negligible hysteresis [10,11]. This system also shows an unusual reentrant structural transition sequence: a reentrant rhombohedral ($R\bar{3}$) $\rightarrow$ triclinic ($P\bar{1}$ at 140 K) $\rightarrow$ rhombohedral ferromagnetic (FM) ($R\bar{3}$ at 70 K). This rare reentrant sequence was suggested to arise from competition between Jahn-teller distortion and magnetism [10,11]. The observed Curie-Weiss moment, 6.16 μ_B, is substantially enhanced from the spin-only value of 4.9 μ_B for a $S = 2$ system. Additionally, the saturated moment is about 5 μ_B from powder neutron-diffraction studies [10,11]. These values are close to those of the case of $S = 2$, $L = 1$, thus requiring a large orbital moment on the $3d$ ion. The latter corresponds to the largest possible orbital moment $M_L = 1 \mu_B$ for the t_{2g}^1 system [5]. Optical spectroscopy measurements show semiconducting behavior with an estimated energy gap of 1.5 eV [12].

Although the generalized gradient approximation (GGA) plus on-site Coulomb repulsion U calculations by Mentré and coworkers provided some preliminary results [10], available information about the electronic structures is still limited. Here we report more extensive density functional theory (DFT) based studies, including correlation and SOC, to uncover the origin of the strong magnetocrystalline anisotropy, Mott transition, and the large orbital moment in BaFe$_2$(PO$_4$)$_2$.

II. CRYSTAL STRUCTURE AND METHODS

Figure 1 shows the rhombohedral structure of the space group $R\bar{3}$ (no. 148), which is observed in both low and high T regimes. In this structure, P ions sit in the center of the Fe honeycomb lattice, but above and below the layer along the $\hat{c}$ direction. The P ions are edge shared with three oxygen ions of the FeO$_6$ octahedra, and form PO$_4$ tetrahedra. The Fe^{2+} layers
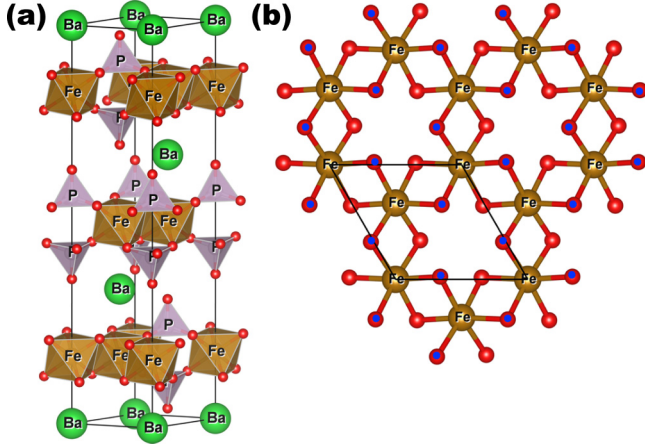
*mckwan@korea.ac.kr
†pickett@physics.ucdavis.edu

FIG. 1. (Color online) (a) The rhombohedral structure, which contains PO_4 tetrahedra and edge-sharing FeO_6 octahedra, of $BaFe_2(PO_4)_2$ in its low and high T regimes. (b) Top view of the two-dimensional Fe honeycomb lattice in the $\hat{a}$-$\hat{b}$ plane. The solid line indicates the unit cell, containing two Fe ions (brown circles). The oxygen ions (small red circles) in the upper layer are denoted by a dot.

are isolated by the intervening insulating $(PO_4)^{3-}$ tetrahedra and Ba^{2+} ions. In the low T phase, the interlayer distance is 7.71 Å along the $\hat{c}$ axis, while the Fe-Fe distance is 2.81 Å. Both structurally and electronically (below), the compound is strongly 2D in nature.

Using the GGA exchange-correlation functional, the internal parameters [13,14] were optimized at the experiment lattice parameters for the low T phase (see Table I), since no experimental data are available. The optimized positions are very similar to the experimental ones at high T, as expected since the difference in volumes between the low and high T phases is only several tenths of a percent [10,11]. The FeO_6 octahedra are somewhat more regular in the low T phase, while the PO_4 tetrahedra are close to an ideal tetrahedron in the high T phase.

TABLE I. Optimized internal parameters and structure information with the experimental lattice parameters of $a = 4.869$ Å and $c = 23.230$ Å at low T [11]. In the representation of a hexagonal lattice, the Ba ions are at $3a$ $(0,0,0)$. The Fe, O1, and P atoms sit at $6c$ $(0,0,z)$, while O2 lies at $18f$ (x,y,z). The O2 ions are corner shared by the PO_4 tetrahedra and the FeO_6 octahedra, whereas the O1 ions are at one of the vertices of the PO_4 tetrahedra. The bond length d and the bond angles are given in units of angstrom and degree, respectively.

	Fe	P	O1	O2		
	z	z	z	x	y	z
Internal parameter	0.1680	0.5710	0.6371	0.3494	0.0235	0.8840
d(Fe-O)($\times 3$)			2.042, 2.050			
d(P-O)			1.536, 1.598($\times 3$)			
$\angle$ O-Fe-O($\times 3$)			86.6, 88.6, 93.2,91.8			
$\angle$ O-P-O ($\times 3$)			107.2, 111.7			

Our calculations were performed in a rhombohedral unit cell with GGA exchange-correlation functional plus U and SOC, which are implemented in the accurate all-electron full-potential code WIEN2K [15], which uses the tetrahedron method for Brillouin-zone integrations. The fully localized limit flavor of the GGA+U functional was used for this strong Fe moment compound. On-site Coulomb repulsion $U = 3$–5 eV and the Hund's exchange parameter $J = 0.70$ eV were employed, as widely used for Fe^{2+} systems [10,16]. The basis size was determined from the smallest atomic sphere by $R_{mt}K_{\max} = 7$ and augmented plane-wave radii of Ba 2.30, Fe 2.00, P 1.61, and O 1.29, in atomic units. The Brillouin zone was sampled up to a k mesh of $21 \times 21 \times 21$ to check convergence carefully in this system, which is nonmetallic at almost all levels of the theory.

III. RESULTS

A. Underlying electronic structure

Before discussing the low-temperature FM phase results, we address the nonmagnetic state, which represents the underlying electronic structure. The enlarged band structure in the energy range of Fe d orbitals and the corresponding densities of states (DOSs) are given in Fig. 2. In the region displayed there are ten d bands, since the unit cell contains two Fe ions. From the tiny oxygen character in the DOS around E_F, we conclude that direct Fe t_{2g}-t_{2g} hopping is substantial due to the edge-sharing octahedral structure, and this interaction leads to a bonding-antibonding splitting $\sim$1 eV of the fully filled t_{2g} manifold. A gap of 0.25 eV opens between the antibonding t_{2g}^* state and the unfilled e_g manifold. This feature of isolated bands around E_F in a hexagonal lattice system is similar to that of the hole-doped superconductor $Li_{1-x}NbO_2$ [17,18]. In both bonding and antibonding manifolds, Dirac points appear at
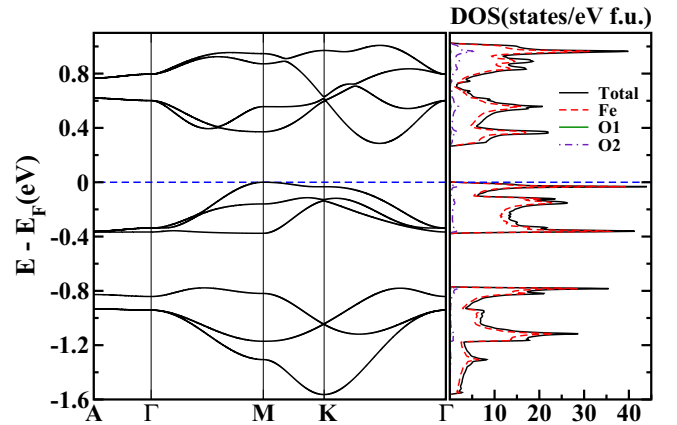

FIG. 2. (Color online) Nonmagnetic GGA band structure (left) and orbital projected densities of states (right) of the rhombohedral structure in the energy region containing Fe d orbitals. Note that the O1 contribution is negligible and invisible here. The occupation confirms the d^6 Fe^{2+} configuration and the density of states just below the gap shows a quasi-one-dimensional character due to the flat band that extends from M to K, hence all around the edge of the Brillouin zone. The bottom of the gap is denoted by the horizontal dashed line. The k-point labels are for the conventional hexagonal lattice, viz. graphene.

the K point by symmetry, as observed in several honeycomb lattices.

An anomalous feature is that the top of the t_{2g}^* manifold (bottom of the gap) is flat along the M-K line, hence along the *entire edge* of the Brillouin zone (which consists of alternating M-K and K-M lines). Considering also the dispersionless character along the $\hat{c}$ axis due to the large interlayer distance, the electronic structure becomes an unusual quasi-one-dimensional one, as evident in the DOS near E_F. This one-dimensionality, however, is not uniaxial but instead radial, perpendicular to the edge of the Brillouin zone. A similar one-dimensionality was found as well in the hexagonal lattice CuAlO$_3$ compound [19].

B. Ferromagnetic electronic structure

1. Uncorrelated electronic structure and magnetism

Now we focus on the FM state, which is the ground state at the low T regime. The magnetic energy is large, with the FM state being 1.2 eV/Fe lower in energy than for the nonmagnetic state. This very large magnetization energy guarantees that the local moment is robust even in the high T disordered regime. Based on the Stoner picture (which may be accurate only for small moments) where this energy is $\frac{1}{4}IM_S^2$, $M_S = 4\,\mu_B$ leads to a broad first estimate of the Stoner I of 0.3 eV. A more realistic means of estimating I is from the band exchange splitting $IM_S = \Delta_{\mathrm{ex}} = 3$ eV of the GGA bands, giving $I = 0.75$ eV, more in line with accepted values for the magnetic 3d ions.

The energies of FM alignment and in-plane antiferromagnetic (AFM) alignment have been compared, varying the value of the on-site repulsion U. For U equal to 3 eV or less, FM alignment is favored. For $U = 4$–5 eV, however, AFM alignment is favored. In this range the orbital occupations for FM alignment do not change, whereas there is some small evolution of orbital occupations for AFM order. The orbital moment is the same large value in all cases. Evidently this question of magnetic alignment is near a delicate balance, so we have not pursued this question of trying to obtain the nearest-neighbor exchange coupling either in plane (which this difference reflects) or out of plane, where coupling should be much smaller and also involves the difficult question of frustrated coupling. We proceed with analysis using the observed FM alignment.

The left side of Fig. 3(a) displays the GGA FM band structure, showing a half-semimetallic character with a minority-spin Dirac point (or Weyl node) [20] lying right below E_F by 30 meV at the point K. The corresponding DOS, given in the right side of Fig. 3(a), shows a $\frac{1}{3}$-filled minority t_{2g} manifold, confirming the high spin $S = 2$ Fe^{2+} configuration. The t_{2g} manifold shows a large exchange splitting of 3 eV. All majority states (t_{2g} and e_g) are filled, hence $\frac{5}{2}$ spin, and orbitally inert. Henceforward we focus on the single minority electron, whose spin half reduces the total spin to $S = 2$ and introduces the question of orbital occupation.

With the local X,Y,Z coordinates of the FeO$_6$ octahedron, the t_{2g} orbitals with global z axis along $\hat{c}$ can be described in a threefold symmetry adapted manner by

$$\phi_m = \frac{1}{\sqrt{3}}\left(\xi_m^0 d_{XY} + \xi_m^1 d_{YZ} + \xi_m^2 d_{ZX}\right), \qquad (1)$$
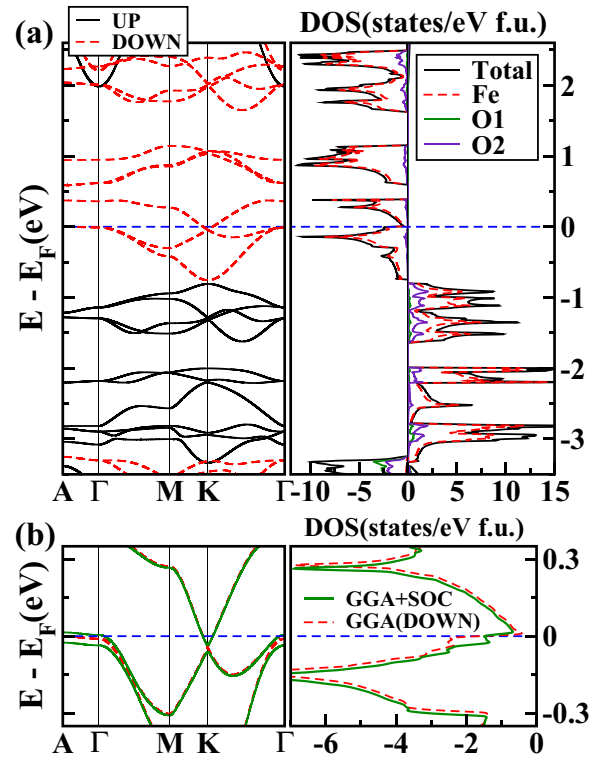

FIG. 3. (Color online) (a) FM band structures and DOSs within GGA in the range of Fe d bands, indicating a half-semimetallic character in the minority bands (red dashed lines). A Dirac point appears almost exactly at E_F at the point K. (b) Overlaid FM GGA (red dashed lines) and GGA+SOC (green solid lines) band structures and total DOS enlarged near E_F, in a ±0.3-eV region containing only some of the minority t_{2g} manifold. The Dirac point is split by about 30 meV by SOC. Note that a tiny hole pocket compensating a tiny electron pocket at the K point appears in a region that is not visible along the lines shown.

where the phase factor is $\xi_m = \exp(i\frac{2\pi m}{3})$, $m = L_z$ is the projection of the orbital moment, and the superscript is an exponent. Due to the small trigonal distortion, the $L_z = 0$ orbital ϕ_0 (d_{z^2} in shape) has a somewhat higher site energy than the doublet $\phi_{\pm1}$. The corresponding DOS near E_F has some similarity to a particle-hole asymmetric version of graphene [21], due to a Dirac point at K that lies very near the Fermi level. The strong magnetism completely changes the Fe ion configuration from $\{t_{2g}^6 e_g^0\}$ to $\{t_{2g}^{3\uparrow} e_g^{2\uparrow} t_{2g}^{1\downarrow}\}$.

2. Dirac point: Semimetal-insulator transition

We now address the observed insulating character of BaFe$_2$(PO$_4$)$_2$, using the GGA+U approach for correlated insulators. Applying a small $U = 1$ eV with $J = 0.5$–1 eV to the Fe ions within GGA+U, the Dirac point degeneracy pins E_F and no gap opens, as shown in Fig. 4(a). The Dirac cone is isotropic, as in graphene. As U is increased, the Dirac point degeneracy continues to pin E$_F$. Applying U up to 7 eV, beyond the limit of a proper value for Fe ions, although higher energy bands shift this system remains a half-semimetal without gap, as illustrated in Figs. 4(b) and 4(c).
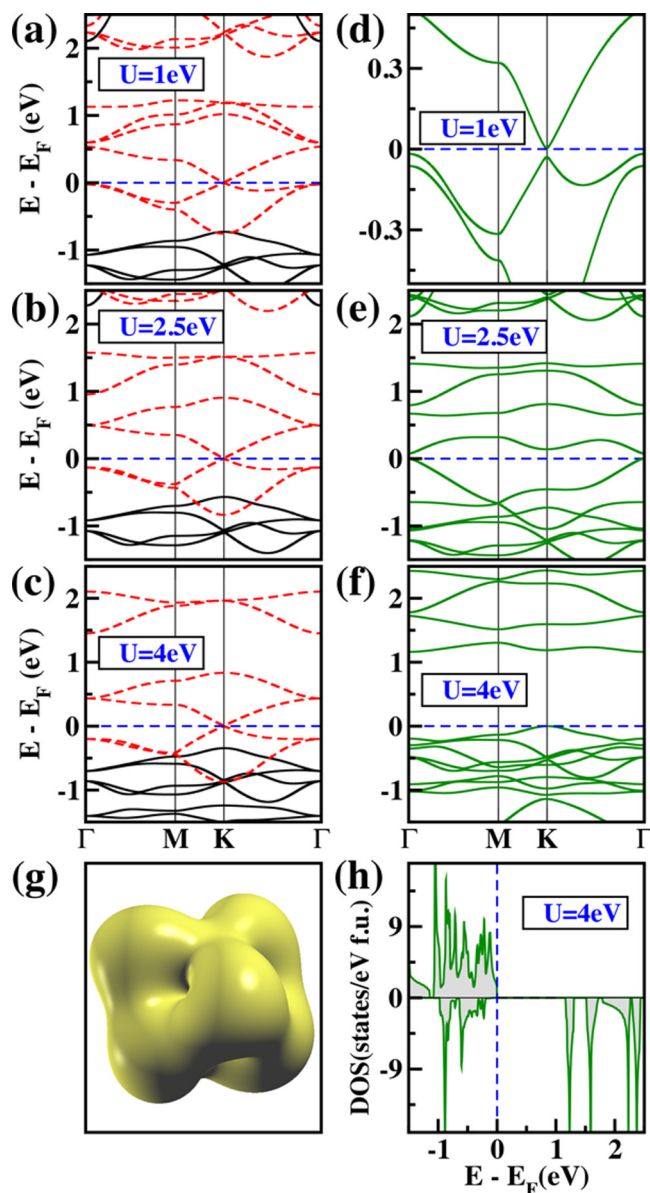
FIG. 4. (Color online) Band structures near E_F (a)–(c) within GGA+U and (d)–(f) from GGA+U+SOC, for $U = 1$–4 eV and $J = 0.7$ eV. The spin-up and -down bands in (a)–(c) are denoted by black solid and red dashed lines, respectively, while the bands including SOC (d)–(f) are shown by green solid lines. In (d) the scale is enlarged to allow the gap opening at the Dirac point to be seen. (g) Charge density plot of the minority d orbitals, shown at the isovalue of 0.09 e/Å^3. The $\hat{c}$ axis is along the vertical direction. This shape is nearly identical for all calculations performed here. (h) Total DOS at $U = 4$ eV in GGA+SOC+U, showing a 1.2-eV energy gap between the corresponding up and down bands.

As mentioned in the Introduction, experiment shows semiconducting behavior and implies a large orbital moment M_L [10,11], which are not explained by GGA+U. We carried out calculations including SOC, both GGA+SOC, and GGA+U+SOC. The GGA+SOC band structure, overlapping the GGA one, is shown in the left panel of Fig. 3(b). SOC leads to a band splitting of 40 meV near E_F, visible in this plot only at the Γ and K points. The linear Dirac bands are also split
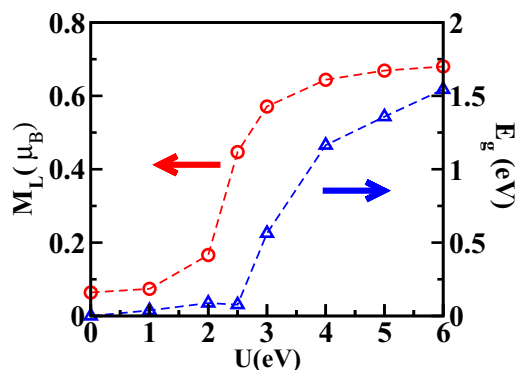

FIG. 5. (Color online) Variation of the Fe orbital M_L moment, and energy gap E_g, varying U in GGA+U+SOC from 0 to 6 eV, with the spin directed along the $\hat{c}$ axis. From $U = 4$ eV, the gap is between the filled spin-up and the unfilled spin-down channels. The critical value of U is in the 2.5–3-eV range.

by 30 meV. This small effect is consistent with the small SOC strength in $3d$ ions, and spin mixing is also degraded by the 2.5-eV exchange splitting.

Another interesting feature occurs in the parabolic bands touching E_F at the Γ point. Inclusion of SOC splits the bands, degenerate at the Γ points, and leaves only one maximum at E_F, which is more isotropic than in the case excluding SOC. As a result, as shown in the DOS of the right side of Fig. 3(b), a van Hove singularity (vHs) appears very near E_F, in addition to two additional vHs at –0.15 and 0.25 eV.

Simultaneous inclusion of correlation and SOC effects splits the Dirac point degeneracy, thereby opening a gap for U as small as 1 eV. At small U this gap is a spin-orbit gap, not a Mott gap. Although the strength of SOC is small in $3d$ systems, the symmetry lowering due to SOC becomes crucial for opening a gap in this system, as occurs also in BaCrO$_3$ [22]. The resulting band structures in GGA+U+SOC are given in Figs. 4(d)–4(f). As displayed in Fig. 5, the energy gap of 1.2 eV for $U = 4$ eV is close to the experimentally estimated value. The gap is indirect, between K and Γ, although due to the small dispersion the direct gap is not much larger. There has been some uncertainty in determining the optical gap spectroscopically [12].

3. Degeneracy lifting and large orbital moment

GGA+SOC gives a negligible magnetocrystalline anisotropy, with an orbital moment of $M_L \approx 0.08\mu_B$/Fe both for in-plane and $\hat{c}$-axis spin alignment. Varying U in GGA+U+SOC with the spin along $\hat{c}$, M_L of Fe rapidly increases in the $U = 2$–3-eV range, then saturates near $0.7\mu_B$ at $U = 4$ eV, as displayed in Fig. 5. This value excludes contributions from the tails of the $3d$ orbitals extending out of the Fe sphere, so the atomic value will be somewhat larger. (This large orbital moment arises for antiferromagnetic alignment as well.) As a critical value U_c of 2.5–3 eV, the opening of a Mott gap begins.

Consistent with the large exchange splitting $\Delta_{ex} = 3$ eV, the total spin moment $M_S = 4\mu_B$/Fe remains unchanged, since mixing of the spin-split orbitals by small SOC is minor. At $U = 4$ eV, the spin direction along the $\hat{c}$ direction has

much lower energy around 400 meV/f.u. than for spin in the $\hat{a}$-$\hat{b}$ plane, explaining the observed Ising behavior. The state obtained for the spin direction in the $\hat{a}$-$\hat{b}$ plane (not pictured) remains semimetallic (Dirac point) even in the large U regime, showing a very small M_L of ∼0.06 μ_B. This striking anisotropy confirms that SOC drives the semimetal-insulator transition, and that depends strongly on spin direction. This type of Ising magnet, i.e., with the spin direction perpendicular to the layers, has been proposed as a crucial ingredient for emergence of a quantum anomalous Hall state [4] in ferromagnets.

We now discuss the origin of the large orbital moment. The SOC operator is

$$H_{\mathrm{SO}} = \xi \vec{S} \cdot \vec{L} = \xi \left[S_z L_z + \frac{1}{2}(S_+ L_- + S_- L_+) \right]. \quad (2)$$

The majority shell is filled, spin split from the active minority orbital by Δ_{ex}, and inert, because spin mixing is reduced by $\xi/\Delta_{\mathrm{ex}} \sim 10^{-2}$. Thus the spin and orbital operators are those of the minority channel. With the majority channel frozen out, the only effect is from the diagonal term $S_z L_z$ with $S_z = -\frac{1}{2}$. For the magnetization along the $\hat{c}$ axis, the orbital degeneracy is broken by $-\frac{\xi}{2}L_z$ for the two orbital projections. With a bandwidth of 0.5 eV, this small splitting induces an orbital moment, but more importantly it specifies the orbital to be occupied in the Mott insulating phase. For the magnetization in plane, the $L_z = \pm 1$ degeneracy remains unbroken, no orbital moment arises, and correlation is ineffective in opening a gap, as discussed above.

As can be seen in Fig. 4(g), the spin-density plot of the filled minority t_{2g} manifold shows the ϕ_{+1} character characteristic of an $L_z = 1$ orbital. When symmetry allows it, the two orbitals $\phi_{\pm 1}$ are equally filled, the semi-Dirac degeneracy remains at K, and so no gap emerges. It is SOC that breaks the degeneracy, which though small enables the correlation effects to operate. Upon increasing U, the single minority electron density begins to transfer from the ϕ_{-1} orbital to the ϕ_{+1} orbital.

IV. DISCUSSION AND SUMMARY

Using the DFT-based calculations, we have investigated the Ising insulating Fe honeycomb lattice system BaFe$_2$(PO$_4$)$_2$, which at the GGA level results in a half-semimetallic electronic structure with a fermionic Dirac point lying nearly precisely at E_F; this degeneracy is split by inclusion of SOC. Applying both U and SOC suppresses the direct t_{2g}-t_{2g} interaction, and leads to a Mott transition of uncommon origin, becoming enabled by the symmetry lowering due to the (small in magnitude) SOC. In the insulating phase the magnetic phase is $S = 2$, $L = 1$. The atomiclike value of L suggests classifying BaFe$_2$(PO$_4$)$_2$ as a $J_{\mathrm{eff}} = 3$ Dirac Mott insulator. These DFT-based studies have explained the large magnetic anisotropy, the very large orbital moment for a 3d ion, and the unusual manner in which spin-orbit coupling enables the Mott gap to open in BaFe$_2$(PO$_4$)$_2$. Even the magnitude of the gap is given reasonably by our methods.

The reentrant structural transitions mentioned in the Introduction need comment. The Fe honeycomb lattice studied here bears a great deal of similarity to the (111)-oriented

perovskite bilayers that are recently being studied [23,24], a difference being that in the latter case the metal-oxygen octahedra are corner sharing rather than edge sharing. In those systems structural symmetry breaking is predicted in some cases, using the same methods as used here. That symmetry breaking involves an unusual type of orbital-occupation competition. The high-symmetry structure (threefold, as here) supports complex-valued, orbital moment containing orbitals, but breaking to low symmetry (*P1* space group in that case) is connected with occupation of t_{2g} type real orbitals adapted to the local pseudocubic symmetry.

The same orbital-occupation competition can be expected in BaFe$_2$(PO$_4$)$_2$. At high temperature where the Fe spins are disordered (primarily up and down due to the Ising nature) the (space- and time-averaged) symmetry is the high threefold symmetry, and the symmetry adapted ϕ_{+1} orbital is occupied and shows up in the Curie-Weiss moment. The "ground state" (with spins still disordered) may be one in which a real valued t_{2g} orbital is ordered instead, with accompanying symmetry lowering, and the transition toward such a lower-symmetry structure occurs at 140 K. However, upon ordering ferromagnetically, the strains that accompany occupation of cubic orbitals (viz. Jahn-Teller strains) may be incompatible with long-range order. Such spin-lattice competition could then favor a return to the symmetric structure at or near the Curie temperature, as observed. Further consideration of this mechanism will be left for future work.

A Dirac point has played an important role in our discussion of how the Mott gap in BaFe$_2$(PO$_4$)$_2$ arises only when spin-orbit coupling is included. Few instances of a Dirac point pinned to the Fermi level in a ferromagnet have been reported, which produces a half-semimetallic system. One such instance is in the CrO$_2$/TiO$_2$ multilayer [25], where it is actually a semi-Dirac semi-Weyl point. Another instance is that of (111)-oriented perovskite superlattices [24,26], where Dirac point degeneracies are only lifted by symmetry-breaking interactions. Related band points arise in the hexagonal W lattice on the Cl-Si surface [4], and are also of interest in triangular lattice systems [27]. In some such systems, Chern bands with a Chern number ± 2 are proposed [25,26]. In addition, the three-dimensional Weyl semimetals NbP and TaAs, which are distinguished by lack of inversion symmetry but preserving time-reversal symmetry, have been very much of interest, since these compounds show an extremely large and unsaturated magnetoresistivity even for very high magnetic field [28–31]. BaFe$_2$(PO$_4$)$_2$ bears some similarity to the above-mentioned compounds, and has the potential for additional interesting properties.

[1] C. L. Kane and E. J. Mele, Z_2 Topological Order and the Quantum Spin Hall Effect, Phys. Rev. Lett. **95**, 146802 (2005).

[2] A. Rüegg and G. A. Fiete, Topological insulators from complex orbital order in transition-metal oxides heterostructures, Phys. Rev. B **84**, 201103(R) (2011).

[3] A. Shitade, H. Katsura, J. Kuneš, X.-L. Qi, S.-C. Zhang, and N. Nagaosa, Quantum Spin Hall Effect in a Transition Metal Oxide Na_2IrO_3, Phys. Rev. Lett. **102**, 256403 (2009).

[4] M. Zhou, Z. Liu, W. Ming, Z. Wang, and F. Liu, sd^2 Graphene: Kagome Band in a Hexagonal Lattice, Phys. Rev. Lett. **113**, 236802 (2014).

[5] K.-W. Lee and W. E. Pickett, Orbital-quenching-induced magnetism in Ba_2NaOsO_6, Europhys. Lett. **80**, 37008 (2007).

[6] S. Gangopadhyay and W. E. Pickett, Spin-orbit coupling, strong correlation, and insulator-metal transitions: The $J_{eff} = 3/2$ ferromagnetic Dirac-Mott insulator Ba_2NaOsO_6, Phys. Rev. B **91**, 045133 (2015).

[7] H. Jin, H. Jeong, T. Ozaki, and J. Yu, Anisotropic exchange interactions of spin-orbit-integrated states in Sr_2IrO_4, Phys. Rev. B **80**, 075112 (2009).

[8] E. Pavarini, S. Biermann, A. Poteryaev, A. I. Lichtenstein, A. Georges, and O. K. Andersen, Mott Transition and Suppression of Orbital Fluctuations in Orthorhombic $3d^1$ Perovskites, Phys. Rev. Lett. **92**, 176403 (2004).

[9] I. G. Rau, S. Baumann, S. Rusponi, F. Donati, S. Stepanow, L. Gragnaniello, J. Dreiser, C. Piamonteze, F. Nolting, S. Gangopadhyay, O. R. Albertini, R. M. Macfarlane, C. P. Lutz, B. A. Jones, P. Gambardella, A. J. Heinrich, and H. Brune, Reaching the magnetic anisotropy limit of a $3d$ metal atom, Science **344**, 988 (2014).

[10] H. Kabbour, R. David, A. Pautrat, H.-J. Koo, M.-H. Whangbo, G. André, and O. Mentré, A genuine two-dimensional Ising ferromagnet with magnetically driven re-entrant transition, Angew. Chem. Int. Ed. **51**, 11745 (2012).

[11] R. David, A. Pautrat, D. Filimonov, H. Kabbour, H. Vezin, M.-H. Whangbo, and O. Mentré, Across the structural re-entrant transition in $BaFe_2(PO_4)_2$: Influence of the two-dimensional ferromagnetism, J. Am. Chem. Soc. **135**, 13023 (2013).

[12] R. David, H. Kabbour, D. Filimonov, M. Huvé, A. Pautrat, and O. Mentré, Reversible topochemical exsolution of iron in $BaFe_2^{2+}(PO_4)_2$, Angew. Chem. Int. Ed. **53**, 13365 (2014).

[13] Using FPLO [14], the internal parameters were optimized, until the forces were less than 1 meV/a.u.

[14] K. Koepernik and H. Eschrig, Full-potential nonorthogonal local-orbital minimum-basis band-structure scheme, Phys. Rev. B **59**, 1743 (1999).

[15] K. Schwarz and P. Blaha, Solid state calculations using WIEN2K, Comput. Mater. Sci. **28**, 259 (2003).

[16] H. J. Xiang, S.-H. Wei, and M.-H. Whangbo, Origin of the Structural and Magnetic Anomalies of the Layered Compound $SrFeO_2$: A Density Functional Investigation, Phys. Rev. Lett. **100**, 167207 (2008).

[17] E. R. Ylvisaker and W. E. Pickett, First-principles study of the electronic and vibrational properties of $LiNbO_2$, Phys. Rev. B **74**, 075104 (2006).

[18] K.-W. Lee, J. Kuneš, R. T. Scalettar, and W. E. Pickett, Correlation effects in the triangular lattice single-band system Li_xNbO_2, Phys. Rev. B **76**, 144513 (2007).

[19] E. R. Ylvisaker and W. E. Pickett, Doping-induced spectral shifts in two-dimensional metal oxides, Europhys. Lett. **101**, 57006 (2013).

[20] X. Wan, A. M. Turner, A. Vishwanath, and S. Y. Savrasov, Topological semimetal and Fermi-arc surface states in the electronic structure of pyrochlore iridates, Phys. Rev. B **83**, 205101 (2011).

[21] R. Nandkishore, L. S. Levitov, and A. V. Chubukov, Chiral superconductivity from repulsive interactions in doped graphene, Nat. Phys. **8**, 158 (2012).

[22] H.-S. Jin, K.-H. Ahn, M.-C. Jung, and K.-W. Lee, Strain and spin-orbit coupling induced orbital ordering in the Mott insulator $BaCrO_3$, Phys. Rev. B **90**, 205124 (2014).

[23] D. Doennig, W. E. Pickett, and R. Pentcheva, Massive Symmetry Breaking in $LaAlO_3/SrTiO_3$(111) Quantum Wells: A Three-Orbital, Strongly Correlated Generalization of Graphene, Phys. Rev. Lett. **111**, 126804 (2013).

[24] D. Doennig, W. E. Pickett, and R. Pentcheva, Confinement-driven transitions between topological and Mott phases in $(LaNiO_3)_N/(LaAlO_3)_M$(111) superlattices, Phys. Rev. B **89**, 121110(R) (2014).

[25] T.-Y. Cai, X. Li, F. Wang, J. Sheng, J. Feng, and C.-D. Gong, Emergent topological and half semimetallic Dirac Fermions at oxide interfaces, arXiv:1310.2471.

[26] A. M. Cook and A. Paramekanti, Double Perovskite Heterostructures: Magnetism, Chern Bands, and Chern Insulators, Phys. Rev. Lett. **113**, 077203 (2014).

[27] Y. Akagi and Y. Motome, Spontaneous formation of kagome network and Dirac half-semimetal on a triangular lattice, Phys. Rev. B **91**, 155132 (2015).

[28] S.-M. Huang, S.-Y. Xu, I. Belopolski, C.-C. Lee, G. Chang, B. Wang, N. Alidoust, G. Bian, M. Neupane, A. Bansil, H. Lin, and M. Z. Hasan, An inversion breaking Weyl semimetal state in the TaAs material class, Nat. Commun. **6**, 7373 (2015).

[29] H. Weng, C. Fang, Z. Fang, B. Andrei Bernevig, and X. Dai, Weyl Semimetal Phase in Noncentrosymmetric Transition Metal Monophosphildes, Phys. Rev. X **5**, 011029 (2015).

[30] C. Shekhar, A. K. Nayak, Y. Sun, M. Schmidt, M. Nicklas, I. Leermakers, U. Zeitler, W. Schnelle, J. Grin, C. Felser, and B. Yan, Extremely large magnetoresistance and ultrahigh mobility in the topological Weyl semimetal NbP, Nat. Phys. **11**, 645 (2015).

[31] K.-H. Ahn, K.-W. Lee, and W. E. Pickett, Spin-orbit interaction driven collective electron-hole excitations in a non-centrosymmetric nodal loop Weyl semimetal, arXiv:1507.03637.